YALE
PEABODY
MUSEUM

JOURNAL OF MARINE RESEARCH

The *Journal of Marine Research,* one of the oldest journals in American marine science, published important peer-reviewed original research on a broad array of topics in physical, biological, and chemical oceanography vital to the academic oceanographic community in the long and rich tradition of the Sears Foundation for Marine Research at Yale University.

An archive of all issues from 1937 to 2021 (Volume 1–79) are available through EliScholar, a digital platform for scholarly publishing provided by Yale University Library at https://elischolar.library.yale.edu/.

Requests for permission to clear rights for use of this content should be directed to the authors, their estates, or other representatives. The *Journal of Marine Research* has no contact information beyond the affiliations listed in the published articles. We ask that you provide attribution to the *Journal of Marine Research.*

Yale University provides access to these materials for educational and research purposes only. Copyright or other proprietary rights to content contained in this document may be held by individuals or entities other than, or in addition to, Yale University. You are solely responsible for determining the ownership of the copyright, and for obtaining permission for your intended use. Yale University makes no warranty that your distribution, reproduction, or other use of these materials will not infringe the rights of third parties.

Convectively driven coastal currents in a rotating basin

by Scott A. Condie[1] and Gregory N. Ivey[1]

ABSTRACT

Density driven coastal currents were produced in the laboratory by differentially heating and cooling the end walls of a rotating rectangular cavity. After turning on the heat flux, intrusions propagated along the side walls of the cavity under an inertial buoyancy balance, with a geostrophic cross-stream balance. These boundary currents were internally stratified in temperature, while the environment during the early stages of development of the flow was isothermal. Rotational instabilities developed on the edge of the currents and broke to form cyclone-anticyclone eddy pairs. Measurements were made of the intrusion velocity, the temporal development of the width of the boundary currents, their internal thermal structure, and the characteristics of the unstable waves, including their growth rates, wavelengths, and phase speeds. Comparisons are made with previous field observations of the Leeuwin Current off Western and Southern Australia.

1. Introduction

Coastal currents driven by temperature or salinity gradients and influenced by the Earth's rotation are common in the oceans. For example, fresh water entering the sea from rivers is deflected to the right (in the Northern hemisphere) by Coriolis forces and moves along the coast. Larger scale ocean currents flowing along continental coastlines are produced by horizontal density gradients and have a significant effect on the global circulation and coastal climates. Notable examples include the East Greenland Current (Wadhams *et al.*, 1979), the Norwegian Coastal Current (Mysak and Schott, 1977), the Alaska Coastal Current (Royer, 1981) and the Leeuwin Current off Western and Southern Australia (Godfrey and Ridgeway, 1985). Many of these currents flow along meridional boundaries and play a significant role in the transport of heat between polar and subpolar or temperate and equatorial regions.

In previous laboratory studies, boundary currents have been produced by releasing a fixed volume of buoyant fluid into a rotating channel. A vertical barrier separating fluids of different densities was removed so that the lighter fluid spread over the heavy fluid and was deflected to the right (for anti-clockwise rotation) by Coriolis forces (see review by Griffiths, 1986). Using this approach Stern *et al.* (1982) observed boundary currents for a range of density differences and rotation rates. In that study, the

currents consisted of an unsteady bulbous head with a thin neck, followed by a quasi-laminar jet along the boundary. The width of the boundary jet, nose velocity and detrainment coefficient (fraction of the boundary transport left behind the propagating nose) were measured. Theoretical values of these quantities, based on a similarity solution, were in reasonable agreement with their experiment. After the flow progressed a short distance from the lock, the nose velocity decreased until eventually the flow either separated from the wall or became stagnant. Griffiths and Hopfinger (1983) quantified this behavior in similar experiments, and identified a decay in both the depth and the velocity of the nose, which was well described by an exponential law. They argued that for currents with Ekman numbers less than 10^{-3} this decay was the result of transfer of momentum into the lower layer by inertial waves excited by turbulent motions near the nose. For larger Ekman numbers the decay was dominated by Ekman dissipation. When the depth and velocity became very small, Griffiths and Hopfinger reported a transition to a shallow viscous intrusion moving slowly along the wall.

Prominent features observed along boundary currents both in nature and in the laboratory are rotationally induced instabilities. These instabilities may have a significant influence on the dynamics and heat transfer of the flow. Rotation tends to inhibit the transport of heat and momentum (except along a side boundary), whereas instability breaks the cross-stream geostrophic constraints and allows these quantities to be redistributed by eddies. Griffiths and Linden (1981, 1982) investigated experimentally the stability of a two layer flow around a vertical cylindrical wall, while Griffiths and Hopfinger (1984) described the development of rotationally dominated turbulence at a density front (such as that formed at the edge of a coastal current). Killworth and Stern (1982) used asymptotic stability analysis to examine the stability of a coastal current forming a density front along its outer edge and flowing above a deep passive layer. They found the flow was unstable provided the mean potential vorticity increased toward the wall. Killworth *et al.* (1984) considered a more realistic geostrophic current for which the lower layer was of finite depth and found the effect of the lower layer was such that the front was always unstable, regardless of the potential vorticity distribution. In that case, the growing waves extracted energy from both vertical (baroclinic) and horizontal (barotropic) velocity shears.

All the studies discussed above are relevant to the present study in certain respects. Our experiments, however, are fundamentally different from earlier work. In contrast to the fixed volume releases, our boundary currents are produced by a continuous source of buoyant fluid and as a result, are internally stratified in temperature. This approach will accommodate observations over longer time scales and is generally more relevant to geophysical flows.

2. Description of the experiments

The experiments were conducted in a rectangular perspex cavity of height $H = 15$ cm, length $L = 200$ cm and width $B = 60$ cm, giving a fixed longitudinal aspect ratio
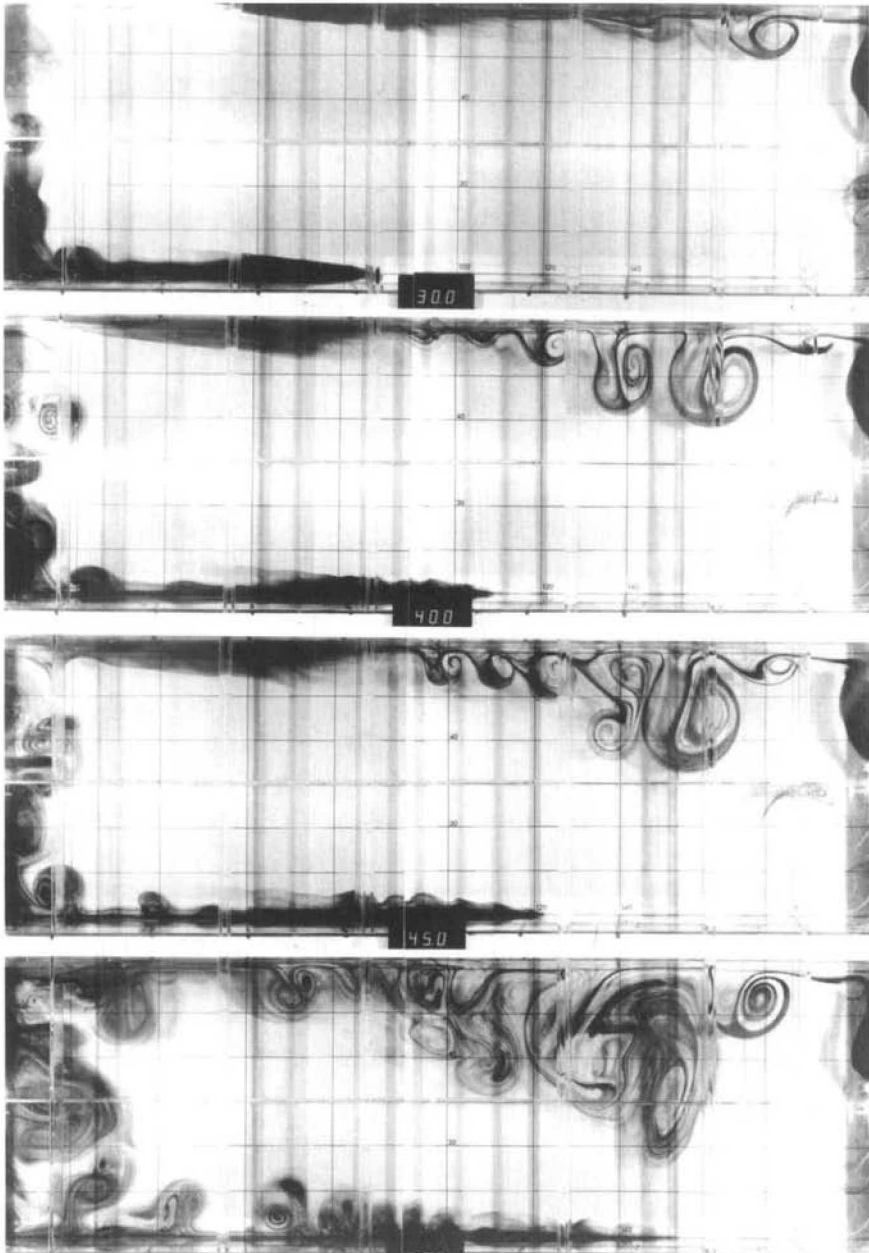
Figure 1. A plan view of the development of the warm and cold boundary current when $f = 1.0\ \text{s}^{-1}$. The hot current flows from the right-hand end wall along the underside of the lid, while the cold current flows from the left along the bottom. The number of rotation periods since the commencement of heating and cooling is displayed at the bottom of the figure. The tank rotation is anti-clockwise.

of A = 0.075. Heat exchangers formed the two vertical end walls of the tank and consisted of a 3.0 cm thick aluminum block with 1.2 cm square grooves through which heated or cooled water was pumped. To ensure an even temperature distribution over the heat exchanger surface, a 1.0 cm thick block of copper was in contact with the working fluid. Thermistors embedded in the copper plates allowed the temperature of the metal in contact with the working fluid to be measured. The tank, which was insulated to minimize heat losses, lay on a sheet of 5 cm thick expanded polystyrene. Heat transfer along the side walls was restricted by air cavities of width 10 cm. The lid, as a potential source of significant heat losses, was designed as a series of sealed transparent air cavities. This assembly was mounted on a 1.0 m diameter rotating table. Fluid slip rings allowed the hot and cold baths supplying fluid to the end walls to be located off the table. Visual facilities included a video camera and recorder, movie camera and still cameras. Active thermistor bridges on the turn table allowed for amplification of thermistor probe signals. The amplified signals passed through electrical connections from the rotating table to the stationary reference frame, where they were recorded.

For each run the tank was filled with water and spun up to solid body rotation with an angular velocity, $f/2$, where f is the Coriolis parameter. Each experiment was initiated by commencing the pumping of hot and cold water through the heat exchangers. This process produced end wall temperatures of $T_0 \pm \Delta T$ for the hot and cold ends respectively, where T_0 was the initial temperature of the working fluid. As the flow from the hot and cold ends was almost symmetric (the only asymmetry was a higher buoyancy flux out of the hot thermal boundary layer due to the nonlinear equation of state of water), it is sufficient to describe the kinematics of the flow which originated from the hot wall. When heating was initiated a thermal boundary layer rapidly formed adjacent to the heated surface. As yet unaffected by rotation, the buoyant fluid rose vertically and was turned into the interior by the upper horizontal lid. Coriolis forces pushed this current to the right (anti-clockwise rotation) and after a transition distance of the order of the internal Rossby radius, a density current formed along the right-hand wall. When $f < 0.2 \text{ s}^{-1}$ a bulbous 'head' structure similar to those in high Reynolds number lock-exchange experiments (Stern *et al.*, 1982; Griffiths and Hopfinger, 1983) was observed. Conversely, at larger rotation speeds the depth of the intrusion increased monotonically from the nose such that the currents did not possess a distinct head structure. Photographs are shown of the development over time of warm and cold intrusions (Fig. 1) and of well developed warm intrusions for a range of rotation speeds (Fig. 2). Figure 2 clearly demonstrates that the boundary currents were narrower at higher rotation speeds. This aspect will be discussed further in Sections 3 and 4 below.

Ten to fifteen rotation periods after the boundary currents were first formed, rotationally induced instabilities developed on their edge some distance behind the nose. These were likely to be mixed mode instabilities with both barotropic and baroclinic components. When $f < 0.5$ the waves were damped, probably by some
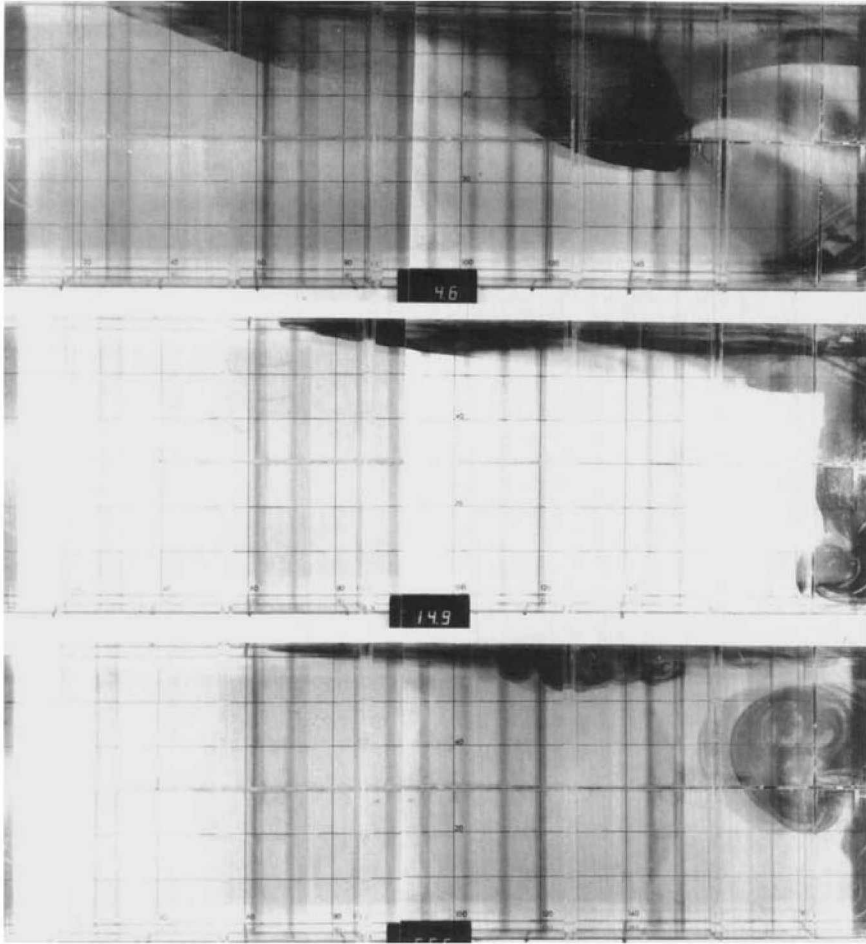
Figure 2. Plan views of the warm boundary currents for $f = 0.1$, 0.5, and 2.0 s^{-1} respectively.

combination of Ekman layer dissipation and the effects of the finite width of the cavity. At higher rotation rates, however, they broke backward toward the source of the intrusion, producing a cyclonic eddy. If unimpeded by neighboring eddies, an anticyclone formed on the downstream side of the cyclonic eddy to create a dipolar eddy pair. Dye streaks also revealed that eddy structures penetrated into the lower layer, sometimes reaching the bottom of the tank. Neighboring eddies interacted in a highly nonlinear fashion, spreading hot fluid laterally across the tank. When the intrusion reached the cold end wall it sunk and some of this fluid became part of the cold boundary current. The coupling of this circulation with the rotational instabilities transferred heat and momentum throughout the fluid until eventually a steady mean state was reached. The flow was then dominated by eddies and at the higher rotation rates included regions of geostrophic turbulence. A detailed account of the steady flow

will be given in a later paper. This paper concentrates on the early period of the experiments in which the intrusion was still distinct from the surrounding fluid (≤ 100 rotation periods).

3. Analysis

A simple scaling analysis can be used to determine the force balances operating in the experiment before instabilities became prominent. It will be shown that much of the dynamics of the intrusion can be described in terms of the Ekman number defined by the relation

$$Ek = \frac{\nu}{h^2 f} \tag{1}$$

where ν is the kinematic viscosity and h is the depth scale of the intrusion. Although it is not usual to include a dependent variable (in this case h) in the definition of a dimensionless parameter, this form of the Ekman number was found to be physically the most appropriate. Results in this form are also more relevant to previous studies of rotating boundary currents, such as Stern *et al.,* 1982 and Griffiths and Hopfinger, 1984 which also included scaling based on the local depth of the intrusions. The dependence of h on the independent variables will be discussed in Section 4 below. For the purposes of this study, we are only interested in the regime in which

$$Ek < 1. \tag{2}$$

If (2) is not satisfied, the problem reduces to the nonrotating case analyzed by Patterson and Imberger (1980) and will not be considered further.

The density of the ambient fluid is denoted by ρ and the pressure by p. The x direction is defined as parallel to the adiabatic side walls and directed from the hot to the cold end of the basin. The y coordinate is normal to these side walls and the z coordinate is vertical, while the corresponding velocity components are (u, v, w) respectively. If the flow is assumed to be parallel to the side boundary, then the x component of the momentum equation for the flow within the intrusion can then be expressed as

$$\frac{Du}{Dt} = -\frac{1}{\rho}\frac{\partial p}{\partial x} - \left(\frac{1}{2}\nu f\right)^{1/2}\frac{\partial u}{\partial z}. \tag{3}$$

The last term parameterizes the dissipation of momentum due to the Ekman layer beneath the fixed lid (Gill, 1982 p. 331). The cross-stream and vertical components of the momentum equation are assumed to be given by the geostrophic and hydrostatic approximations

$$fu = -\frac{1}{\rho}\frac{\partial p}{\partial y}, \tag{4}$$

$$0 = -\frac{1}{\rho}\frac{\partial p}{\partial z} + g', \tag{5}$$

where $g' = g\alpha(T - T_0)$ is the reduced gravity, α is the coefficient of thermal expansion and T is the local temperature.

The longitudinal pressure gradient term in Eq. (3) represents the buoyancy driving of the flow and therefore can always be assumed to be significant. Comparing the inertial and Ekman dissipation terms in (3) indicates that the inertial term will dominate for times less than the spin-down time

$$\tau \sim \frac{h}{\left(\frac{1}{2}\nu f\right)^{1/2}}. \tag{6}$$

Therefore, when $t < \tau$ the alongshore balance is between buoyancy and inertial terms. This gives the internal wave speed as a velocity scale

$$U \sim Nh, \tag{7}$$

while (4) and (5) imply that the cross-stream width b scales with the internal Rossby deformation radius R:

$$b \sim R = \frac{Nh}{f} \tag{8}$$

where the buoyancy frequency is defined by the relation $N = [g\alpha(\partial T/\partial z)]^{1/2}$. Eq. (8) can alternatively be expressed as a scale for the slope of isotherms within the current

$$\frac{\partial h}{\partial y} \sim \frac{h}{R} \sim \frac{f}{N}. \tag{9}$$

For times larger than the spin-down time, the scaling indicates that the inertial term will be smaller than the Ekman dissipation term, leaving a balance between buoyancy and Ekman dissipation. The velocity and cross-stream length scales after the transition are given by

$$U \sim Ek^{-1/2}\left(\frac{N^2h^2}{f}\right)x^{-1} \tag{10}$$

and

$$b \sim Ek^{1/2}x. \tag{11}$$

These are overall scales for the flow and are not necessarily applicable near the nose of the intrusion. A balance between buoyancy and inertia may persist in this region until the flow changes to a viscous intrusion. However, if momentum is dissipated over most of the intrusion length the volume transport into the nose region will be reduced. The

depth of the head will subsequently decrease with a corresponding fall in nose velocity.

Instabilities are observed on the edge of the current when it is approximately ten rotation periods old. These instabilities introduce significant cross-stream mass and momentum transfer, which may reduce the volume flux into the nose region and thus cause a reduction in nose velocity. If we assume that this decay mechanism will dominate after eddies have had time to develop (~10 rotation periods), then the intermediate Ekman dissipation regime will play a significant role only if the spin-down is less than order ten rotation periods. This condition corresponds to

$$Ek > 10^{-4}. \tag{12}$$

If (12) is not satisfied, the intrusion may pass from a buoyancy-inertial balance directly to a regime in which buoyancy is balanced by an eddy drag.

The analysis can be extended to take into account the dimensions of the cavity. Dissipation in Ekman layers will play a significant role within the cavity length only if the advective time-scale L/Nh is greater than the spin-down time. This implies that

$$Ek > Fr^{-1} \tag{13}$$

where the rotating Froude number is defined by the relation

$$Fr = \frac{L^2}{R^2} = \left(\frac{fL}{Nh}\right)^2. \tag{14}$$

Therefore, Ekman dissipation will be important only if both (12) and (13) are satisfied. Alternatively, for instability induced drag to be important before the intrusion reaches the end of the tank, L/Nh must be greater than ~10 rotation periods. This in turn requires that

$$Fr > 10^4. \tag{15}$$

The effect of the finite width of the cavity must also be considered. To produce boundary currents analogous to those along continental coastlines, it is essential that the left-hand boundary does not significantly affect the initial intrusion along the right-hand boundary. This requirement can be expressed as a constraint on the ratio of the two relevant horizontal length scales (which takes the form of another Froude number),

$$Fr^* = \frac{B^2}{R^2} = \left(\frac{fB}{Nh}\right)^2 > 1. \tag{16}$$

All of the experimental runs described in this paper, with the exception of a nonrotating run, satisfied condition (16).

The predictions of the scaling analysis can be conveniently summarized in the following form. The intrusion will propagate under an inertial-buoyancy balance over
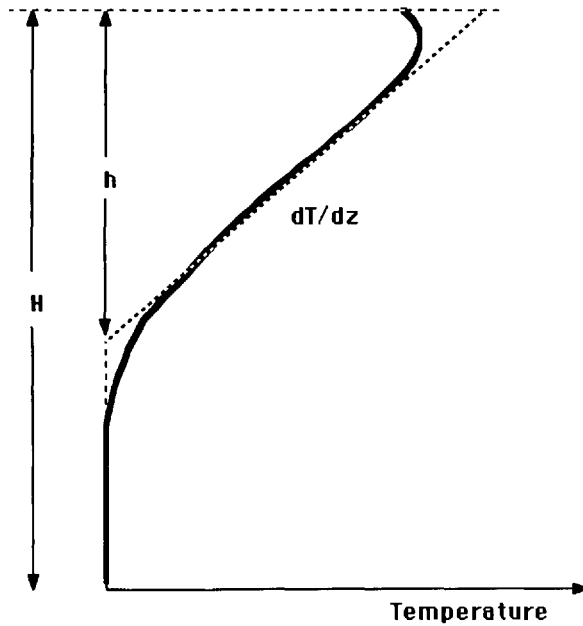
Figure 3. Typical vertical temperature structure of the flow next to the right-hand boundary. This illustrates how both the temperature gradient and depth of the current were defined.

the entire cavity length if

$$\max \{Ek, 10^{-4}\} < Fr^{-1}. \tag{17}$$

The inertial regime is followed directly by a flow dominated by the drag associated with rotational instabilities provided

$$\max \{Ek, Fr^{-1}\} < 10^{-4}. \tag{18}$$

Alternatively when

$$\max \{Fr^{-1}, 10^{-4}\} < Ek, \tag{19}$$

the inertial regime is followed by a period dominated by Ekman dissipation and then another dominated by the instability drag.

4. Results

In this section, the thermal structure of the flow is examined. The alongshore propagation of the current is then considered, including a comparison with some of the theoretical results in Section 3. Properties of the instabilities are discussed in Section 5.

The temperature structure of the boundary currents was investigated using a rack of 15 fast response thermistors at 2.0 cm horizontal spacings. This configuration was
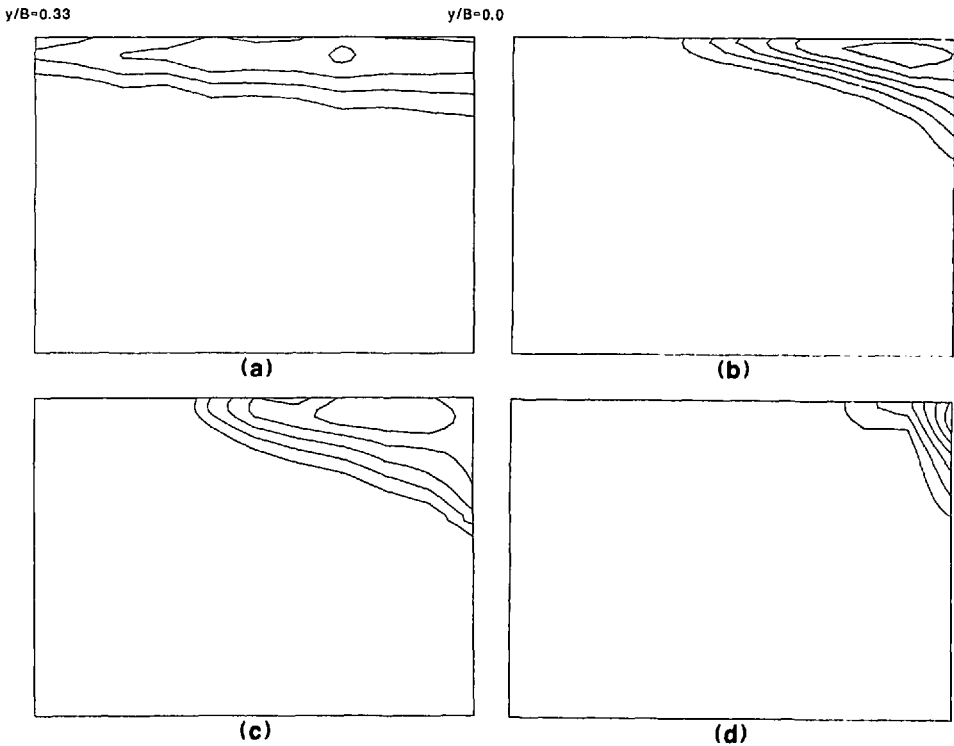
y/B=0.33   y/B=0.0

Figure 4. The cross-stream temperature structure of the warm boundary currents before instabilities appeared at the position of the thermistors ($x = 85$ cm) for $\Delta T = 8°$C. Cross-sections correspond to $f = 0.1, 0.5, 1.0,$ and 2.0 s^{-1} respectively. Isotherms are at 0.5 C intervals while the area over which the profiles were taken is 15 cm high (the full height of the cavity), 20 cm wide (one third of the width of the cavity) and adjacent to the right-hand side boundary.

mounted on a traversing mechanism 85 cm from the heated end wall. Cross-stream profiles covering half the width of the cavity were recorded regularly throughout the duration of each experiment. The profile obtained from the first thermistor (1.0 cm from the side wall) was used to measure the temperature gradient and depth h (see Fig. 3 for a precise definition of these quantities). The precise position at which $\partial T/\partial z$ was measured was not critical, since this quantity was relatively constant across the width of the current. On the other hand, the depth was essentially the maximum depth of the boundary current at that particular cross-section.

Typical cross-sections of the temperature structure of the boundary currents are shown in Figure 4 for a range of rotation rates. The intrusion took a wedge-shaped form which was constrained more tightly to the side boundary as the rotation rate was increased. The shape of the cross-sections of the currents can generally be approximated by the hyperbolic form $h(y) \propto [1 - (\cosh y/R)/(\cosh b/R)]$ predicted by Griffiths and Linden (1982) for a flow of uniform potential vorticity. An average depth
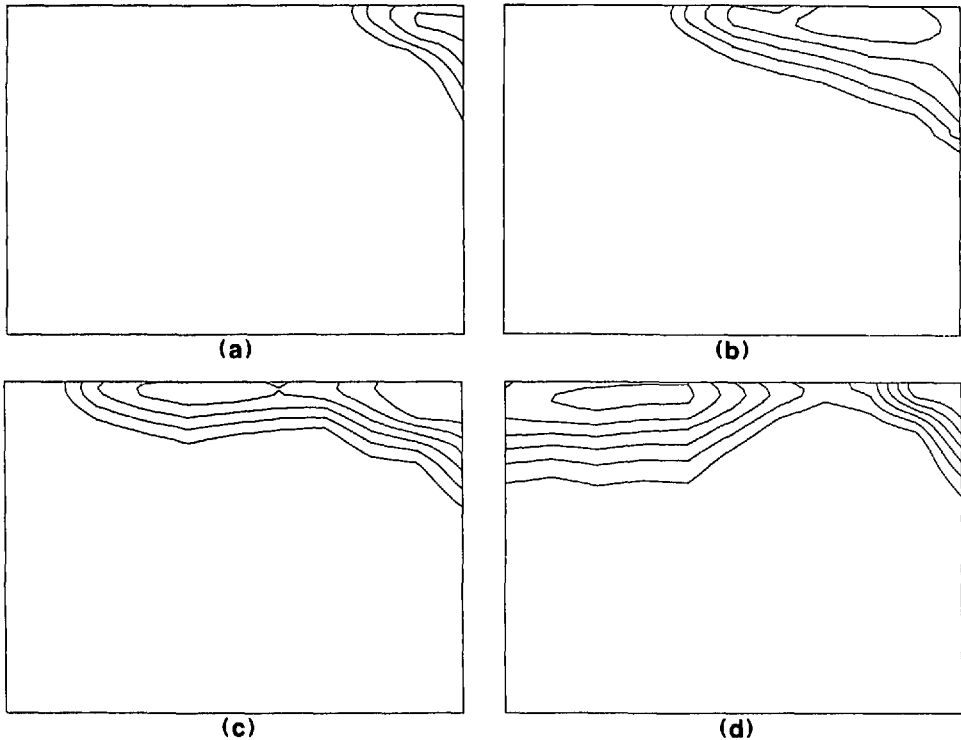
Figure 5. Development of the temperature structure of the warm intrusion with time ($f = 1.0\,s^{-1}$, $\Delta T = 8°C$). The cross-section is the same as that in Figure 4 ($x = 85$ cm). Cross-sections were recorded at 27, 42, 69, and 91 rotation periods after heating commenced. The approximate stage of development of the current for each profile can be determined by referring to the photographs in Figure 1.

of the intrusion $\hat{h}$ can then be defined by $\hat{h} = 1/b \int h(y)dy = 0.7$ h. In many instances the average depth was more relevant in making comparisons with earlier work. Figure 5 illustrates how the geostrophic constraint was broken by instabilities and the subsequent cross-stream spreading by eddies. The latter profiles (5c and 5d) include an anticyclonic eddy whose core took the lens shaped form observed in ocean eddies (Robinson, 1983).

Since the depth and vertical temperature gradient were included in the definition of the parameters Ek and Fr which describe the flow, it is important to describe the dependence of those quantities on the independent variables ΔT and f. Firstly, the temperature gradient was found to be well represented by $\partial T/\partial z \approx \Delta T/2h$, leaving only the dependence of h to be determined. An analysis by Condie and Ivey (1986) in which both dissipation and instability were excluded, indicated that $h \sim (B^4 H^3 \kappa^3/g^3 \alpha^3 \nu)^{1/8} f^{1/2}/\Delta T^{3/8}$. However, only the relatively small range of temperature differences examined ($\Delta T = 6$ to 12°C) there was no significant variation
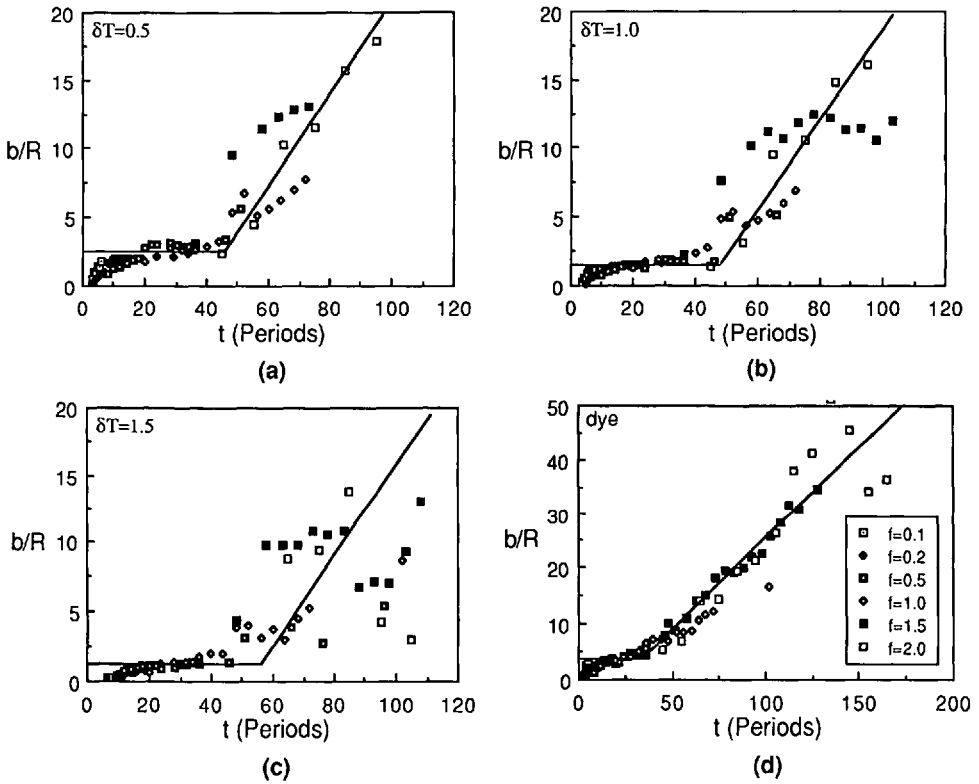
Figure 6. Nondimensional width of the intrusion (at $x = 85$ cm) as a function of time for $\Delta T = 8°C$. The width is defined for the first three graphs as the distance from the boundary to the chosen isotherm ($\delta T = 0.5°C$, $1.0°C$, and $1.5°C$ above ambient temperature for (a), (b) and (c) respectively where the maximum δT in the intrusion is $4.0°C$). Graph (d) corresponds to the width of the dye cloud and includes the definition of the symbols.

in h. Furthermore, when f was increased by a factor of 20 ($f = 0.1$ to 2.0 s^{-1}), h only increased from 6 to 9 cm. These limited observations suggest that the finite depth of the cavity may have influenced the current depth.

As a measure of the current width, the distance of a given isotherm from the side wall was recorded as a function of time from the temperature profiles. The temporal development of the width (nondimensionalized by the internal deformation radius given in Eq. 8) is illustrated by Figure 6. This begins with an initial adjustment period of approximately ten rotation periods. From 10 to 40 rotation periods the current width is relatively constant. Within this time interval the surface width of the isotherm 0.5°C above ambient (where the maximum temperature within the current is 4°C above ambient) is given by $b/R = 2.4 \pm 0.5$ (Fig. 6a). During this period each isotherm for each rotation rate exhibited a similar trend. After 40 rotation periods photographic records reveal that instabilities became visible at the position of the thermistors ($x =$
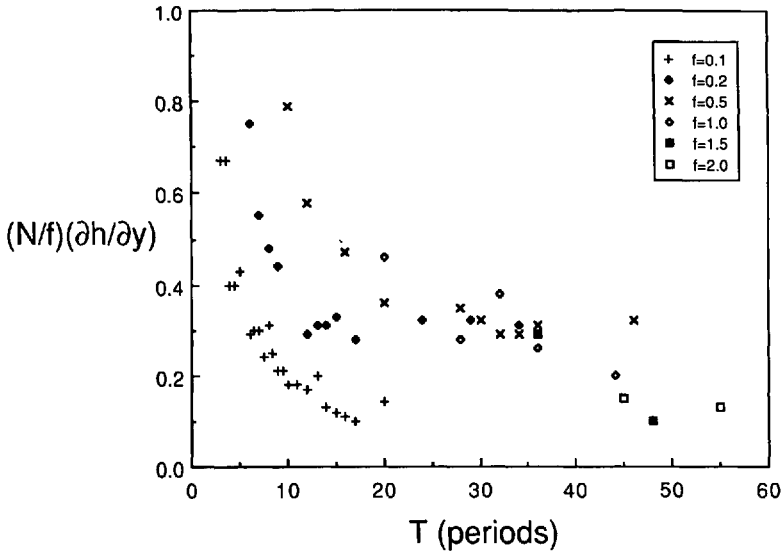
Figure 7. The slope of isotherms as a function of time.

85 cm). From this point the nondimensional width shows a great deal of variation due to the instabilities.

The trends of the previous paragraph are consistent with measurements of the width of the dye clouds at the same cross-section (Fig. 6d). These data are more extensive than the temperature measurements since the latter is restricted to half the width of the tank. The stable period ($t < 40$ rotation periods) corresponds to $b/R = 3.22 \pm 0.30$ for the dye cloud, while the eddy induced spreading ($t > 40$ rotation periods) is well represented by $\partial b/\partial t = 0.33$ deformation radii per period. It is clear that this linear spreading law cannot be maintained indefinitely as the front moves away from its momentum source. Presumably, if the process could be continued for longer times (before the opposite side boundary was encountered), the spreading law would have decay to $t^{1/2}$ consistent with the diffusive spreading of a geostrophically turbulent flow field (Griffiths and Hopfinger, 1984; Ivey, 1987).

While boundary current width measurements form a valuable comparison with satellite images (see for example Griffiths and Pearce, 1985), the slope of isopycnals within the current is a more accessible statistic to ship-based oceanographers. Therefore, for each profile the slopes of isotherms (at 0.5°C intervals) were measured and averaged. Isotherm slopes (nondimensionalized in accordance with Eq. 9) are plotted as a function of time in Figure 7. The slopes can be measured when the isotherms are fairly linear, but not when the temperature structure is more complex (for example Fig. 5d). While the data are thus restricted to relatively short times, the trends are consistent with the width measurements. After an initial adjustment period ($t \leq 10$ rotation periods) the isotherm slope remained relatively constant from 10 to 40
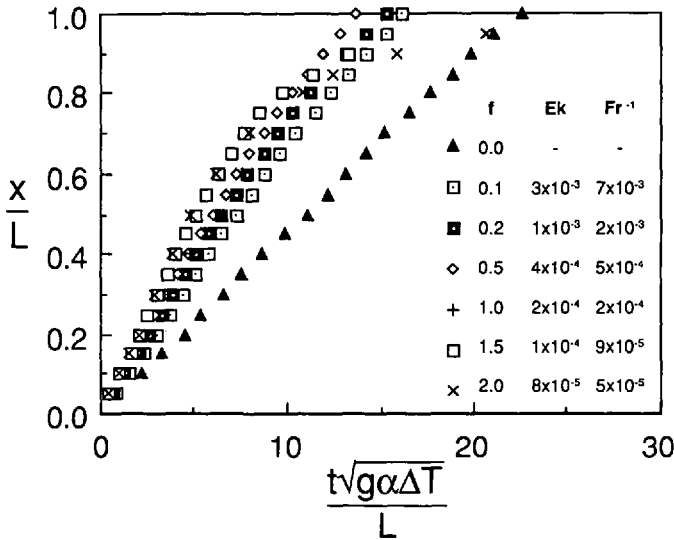
Figure 8. The position of the nose of the intrusion nondimensionalized by the length of the cavity, as a function of time t. Time is nondimensionalized by a term representative of the forcing by the heated and cooled end walls of the cavity. In all runs the end wall temperatures differed from the initial fluid temperature by $\Delta T = 8°C$.

rotation periods and within this interval $\partial h/\partial y = -(0.28 \pm 0.08) f/N$. The values for $f = 0.1$ are anomalously low, perhaps reflecting the influence of the opposite side boundary when $R/B \gtrsim 1$. After 40 periods the intrusions spread by the action of eddies, resulting in a further flattening of the isotherms.

Some of the predictions made in Section 3 were tested by examining the propagation of the head of the intrusion. The distance x the intrusion traveled along the tank was measured as a function of time for a range of rotation speeds. This length was plotted as a function of time t' after the commencement of the experiment for each rotation rate and a virtual time origin t_0 defined such that $t = 0$ when $x = 0$, where $t = t' - t_0$. The nondimensionalized nose position is plotted as a function of nondimensional time in Figure 8. For each rotation rate the initial motion involved a constant nose velocity, consistent with an inertial buoyancy balance. The initial nose velocity also increased with rotation rate. An increase in rotation rate caused a deepening of the intrusion depth, resulting in greater buoyancy forces and the higher velocities observed (as described by Eq. 7).

Figure 8 also reveals a decay of the nose velocity. This effect was more acute, and occurred earlier, at high rotation rates. The decay mechanism is unlikely to be that proposed by Griffiths and Hopfinger (1983) since the three dimensional turbulence which produced the inertial waves in their experiments was absent in our lower Reynolds number currents. As the temporal range of the data was insufficient to quantify the decay, further observations were made. Dye streaks released ahead of the
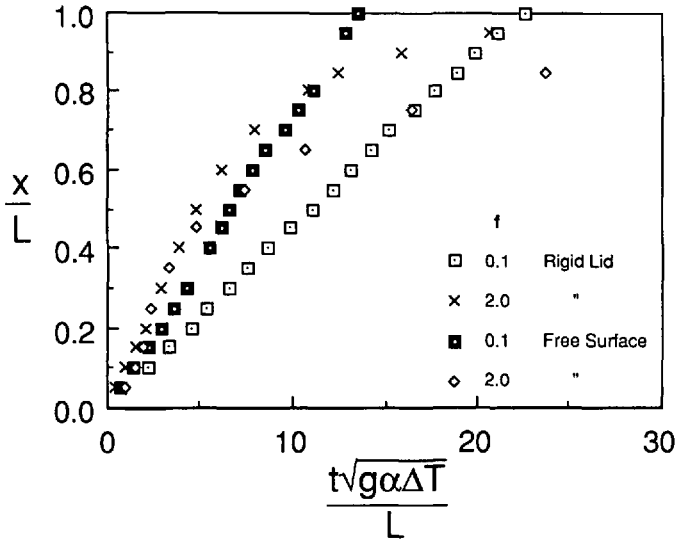
Figure 9. The nose position as a function of time for both fixed lid and free surface experiments ($\Delta T \approx 8°C$).

intrusion revealed neither communication with the approaching end wall nor the presence of inertial waves. Furthermore, temperature measurements at different locations along the side wall revealed that losses in buoyancy due to mixing near the front could only account for a velocity drop of 5 to 10%. This left the two decay mechanisms discussed in Section 3: the dissipation of momentum by Ekman pumping and the essentially inviscid drag associated with rotationally induced instabilities.

A second series of experiments was conducted to identify the dominant decay mechanism. This involved a slight reduction in fluid level in the cavity so as to produce a free surface. The results for $f = 0.1$ s^{-1} and $f = 2.0$ s^{-1} for both fixed lid and free surface experiments are shown in Figure 9. At the low rotation rate ($Ek = 3 \times 10^{-3}$) the initial velocity was higher and the decay almost absent when using a free surface. This result indicates that any velocity decay observed with a fixed lid at this Ekman number was due to Ekman layer dissipation. These observations are consistent with the scaling analysis results in Section 3. On the other hand, intrusions in experiments with a higher rotation rate ($Ek = 8 \times 10^{-5}$) underwent a more rapid velocity decay with a free surface than with a fixed lid. It was also observed that the growth rates of instabilities was greater in the free surface cases (as a result of less Ekman dissipation). Those two observations suggest that the drag at this smaller Ekman number was that associated with the growth of instabilities as predicted in Section 3 (Eq. 18).

Thus to summarize, the experiments like the theory suggest two regimes of propagation. When $Ek > 10^{-4}$ the velocity decay resulted from dissipation within the Ekman layer. Conversely, when $Ek < 10^{-4}$ transfer of mass and momentum away from
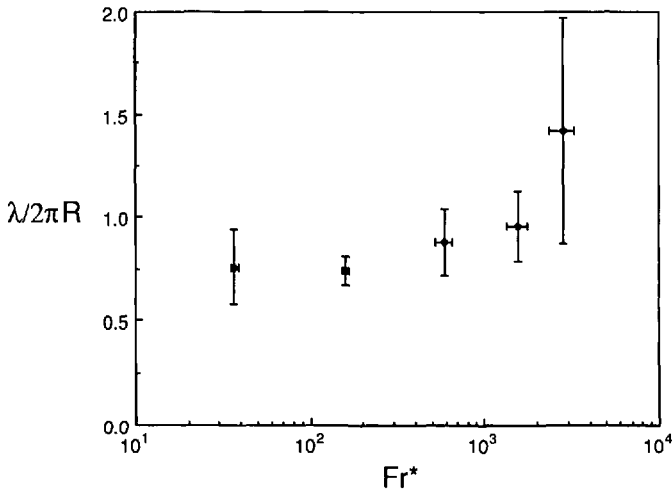
Figure 10. The wavelength of instabilities as a function of Froude number. The error bars represent one standard deviation based on from five to nine measurements (for each Fr^* value) taken at different times and positions in the tank.

the boundary by waves and eddies reduced the alongshore velocity by decreasing the buoyancy flux into the nose region.

5. Instabilities

Rotationally induced instabilities can have a very significant influence on boundary currents. The previous section demonstrated their role in broadening the intrusion and in the decay of the nose speed. We now examine some specific characteristics of those structures such as wavelengths, phase-speeds and growth rates, with emphasis on the small amplitude behavior. At larger amplitudes waves and eddies interacted in a highly nonlinear fashion, making quantitative measurements difficult to interpret.

Wavelengths of small amplitude instabilities were estimated from photographs of the dyed intrusion for a range of rotation rates. The wavelength is here defined as the distance between finite amplitude perturbations on the edge of the current and is nondimensionalized by $2\pi R$ where R is the local value of the internal Rossby radius (defined by Eq. 8). This is plotted as a function of the local Froude number Fr^* (defined by Eq. 16) in Figure 10. The graph confirms that the wavelength scales with the Rossby radius. When $f = 2.0$ s^{-1} ($Fr^* = 3000$), perturbations on the edge of the current grew and interacted very quickly, making small amplitude measurements difficult and hence produced a large degree of scatter in the data. Taking an average of the remaining points gives $\lambda/2\pi R = 0.83 \pm 0.11$ or alternatively $\lambda/2\pi \hat{R} = 1.19 \pm 0.16$ where $\hat{R} = N\hat{h}/f$. The latter figure is the more appropriate for comparison with earlier studies of two layered flows in which the Rossby radius represented a geometric mean
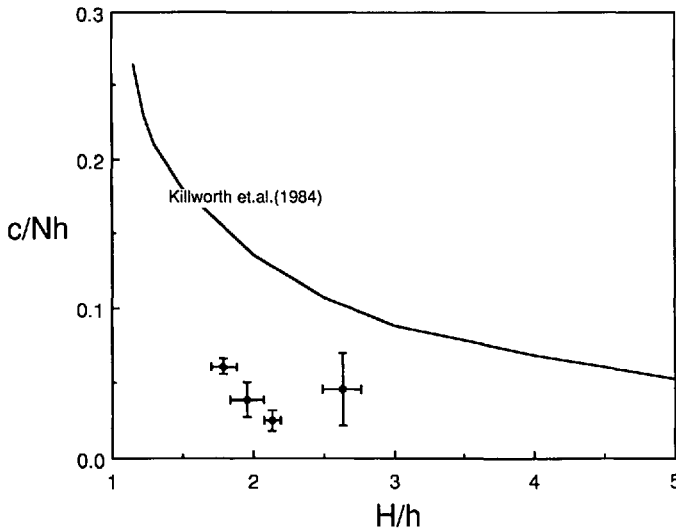
Figure 11. The phase speed of small amplitude instabilities as a function of the depth ratio H/h. Also shown is the theoretical curve predicted by Killworth *et al.* (1984).

for the two layers. The wavelength is similar to the experimental values of 1.1 ± 0.3 found by Griffiths and Linden (1982), 1.16 ± 0.27 by Chia *et al.* (1982) and 1.14 by Narimousa and Maxworthy (1987). It is also in agreement with the theoretical figure of 1.15 derived by Killworth *et al.* (1984) for waves which extract energy from both the vertical and horizontal velocity shears. This suggests that the laboratory waves also had both baroclinic and barotropic components.

Perturbations on the edge of the currents were advected along at finite phase velocities. However, as indicated in Figure 11, these velocities were much less than fluid velocities within the intrusion which were typically of the order of the internal wave speed Nh. The theoretical values of Killworth *et al.* (1984) for a similar current are also illustrated in Figure 11. The experimental phase speeds are typically one third of the theoretical values. Some discrepancy is to be expected since Killworth *et al.* assumed that there was no mean flow in the lower layer. In the experiments, however, the intrusion caused a significant shallowing of the lower layer. In order to conserve potential vorticity in this layer a counter flow was therefore produced beneath the boundary current. This counter current was clearly observed during the experiments using the thymol blue technique (Fig. 12). Since waves interacted with the lower layer, the counter flow would have reduced their forward propagation. Large amplitude eddies, which also must have strongly interacted with the lower layer, had no observable phase velocity. Any movement of these structures was generally not parallel to the boundary and resulted from interactions with other eddies.

The growth rates of waves were also examined. This involved tracking individual waves on photographic records and measuring their cross-stream amplitude ϵ before
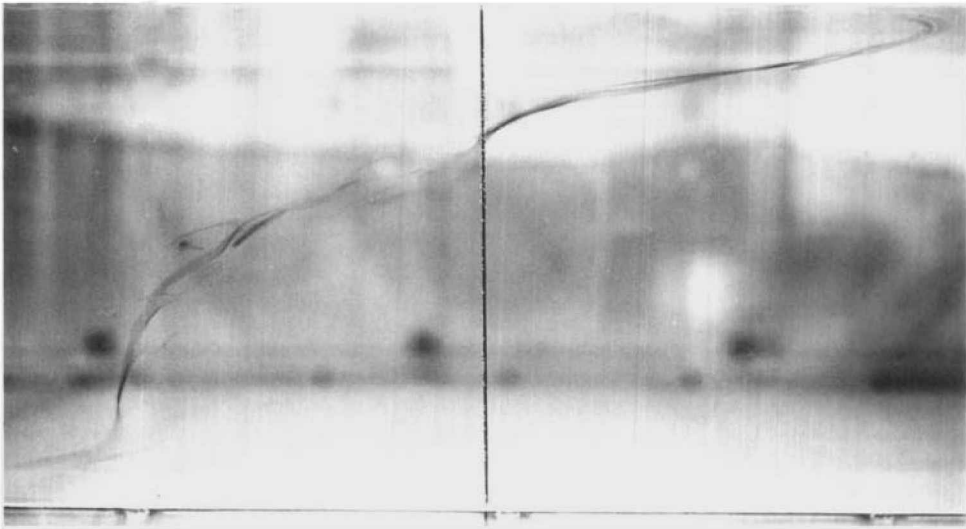
Figure 12. A velocity profile recorded 1.0 cm from the right-hand side boundary by applying a voltage to a vertical wire in a titrated thymol blue solution. The main boundary current is moving to the right of the vertical wire (which represents $u = 0$), while the counter flow beneath is to the left.

they broke or interacted with other waves or eddies. The dominant growth behavior observed during this period was linear. No evidence was found for the exponential growth predicted by linear stability analysis suggesting that this behavior had ceased before the instabilities were large enough to observe. The growth rate during the linear growth period is plotted as a function of Froude number in Figure 13. Although there is generally a small increase in growth rate with Fr^* the trend is not significant when errors are taken into account. Taking an average of these data points gives a nondimensional growth rate for waves beneath a rigid lid of $\epsilon/fR = 0.016 \pm 0.005$. If we assume that the linear behavior dominated throughout the growth of a wave, then a timescale for the growth can be defined as $\lambda/\epsilon = 26 \pm 11$ rotation periods.

After waves had grown to large amplitude they generally broke to form eddies. However, at low rotation speeds the waves were damped and failed to break (see for example the top photograph in Fig. 2). Since eddies can substantially influence the flow, it is important to identify the conditions under which breaking occurs. It is thought that damping was due primarily to the presence of the side boundary opposite the current. Waves were observed to break only when the wavelength $2\pi R$ was less than the width of the cavity. In terms of the Froude number this condition can be expressed as $Fr^* > 4\pi^2$. Dissipation may also have played a significant role in preventing breaking and the experiments indicated that breaking only occurred when
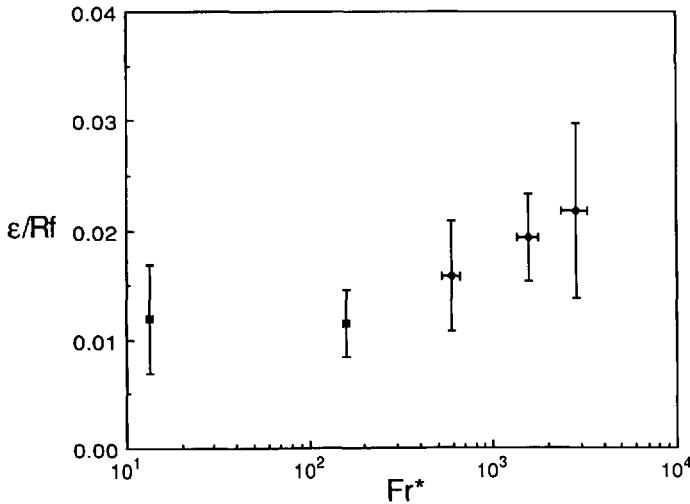
Figure 13. The nondimensionalized growth rate of small amplitude instabilities as a function of Froude number.

$Ek < 10^{-3}$. These results may be relevant to partially enclosed water bodies such as gulfs and straits.

6. Comparison with ocean data

Quantitative comparisons will now be made with field data, with special attention to the Leeuwin Current. This flow consists of a seasonal intrusion of tropical water that moves southward along the Western Australian coast and turns at Cape Leeuwin to flow along the South coast. Thompson (1984) and Godfrey and Ridgeway (1985) showed that the current is driven into the prevailing winds by an alongshore temperature gradient and hence may be compared with the buoyantly driven currents in this study. Since the laboratory experiments did not include a β-effect, they may be particularly representative of the eastward flow along the South coast.

Thompson (1984) presented a hydrographic section of the Leeuwin Current at 25°24′S (Thompson's Fig. 2a). Like the experiments, the vertical temperature gradient showed little variation off the shelf, but was considerably more complex above the shelf. The cross-stream slope of the isopycnals over this section can be expressed as $\partial h/\partial y = -0.25 f/N$ where N is the buoyancy frequency at the shelf edge. This result is in close agreement with the experimental results which gave the constant as 0.28 ± 0.08. Griffiths and Pearce (1985) measured the surface width of the current (from the coast to the center of the main front) from satellite imagery off Australia's South coast. The values obtained for the nondimensional width over a three month period were $b/R \approx 4.1 \pm 1.3$, 3.8 ± 1.0 and 4.8 ± 1.8 for Cape Leeuwin (115E), Albany (118E) and

Hood Point (119.5E) respectively, where the deformation radius was based on the local surface density difference across the front and a maximum current depth of 200 m. In the laboratory experiments, temperature profiles indicated that the edge of the dye cloud may be reasonably representative of the main front. When no large scale wave structures were present the dye gave a nondimensional current width of 3.22 ± 0.30. The tendency of the field values to be slightly higher than the experimental values may result from the difference in the definition of the deformation radius or alternatively, may reflect the presence of the shelf. Ou (1983) found that a shelf in a simple two layered geostrophic adjustment model marginally widened the frontal zone. A third possibility is that instabilities had already influenced the width of the Leeuwin Current. This is quite likely since the satellite images were taken more than a month after the nose of the warm seasonal intrusion had passed the observation point.

Characteristics of instabilities on the Leeuwin Current have also been studied with the aid of satellite images. Griffiths and Pearce (1985) made measurements of the diameters of the major eddy structures and their separation (or wavelength). The values of these two quantities was essentially equal during the early stages of the experiments since eddies grew until they were in contact with neighboring eddies. They then interacted, with the dominant eddy tearing its neighbor apart (see Fig. 1). The diameter of structures off the southern coast of Australia was reported to be $d/2\pi R = 1.19 \pm 0.14$ which is almost identical to the experimental value of 1.19 ± 0.16. The separation of the Leeuwin Current eddies was, however, substantially greater at $\lambda/2\pi R = 2.18 \pm 0.53$. This result may be due to the fact that the field data are related to large amplitude eddies. Griffiths and Pearce (1985) suggested that the wide separation was the result of large meanders engulfing smaller amplitude structures and other nonlinear interactions between different wavelengths such as those discussed by Ikeda *et al.* (1984). Similar behavior was observed during the experiments after ~50 rotation periods (see Fig. 1). The separation of the dominant coherent structures was then quite variable, but always larger than at earlier times.

The phase speeds of all waves observed by Griffiths and Pearce (1985) satisfied $c/Nh < 10^{-2}$ relative to the coast with effectively zero phase speed for large scale eddies. The Leeuwin Current's depth ratio is $H/h \approx 10$, which is considerably larger than the experimental range. However, if the trend in the theoretical curve in Figure 11 is relevant to the experiments, nondimensional phase speeds of order 10^{-2} or less would indeed be expected at such large depth ratios. Despite the smaller depth ratios in the experiment, large scale eddies generally had zero phase velocities as observed on the Leeuwin Current.

The time lapse between the appearance of a small amplitude wave and its breaking to form a dipolar structure, was 10 to 15 rotation periods for both the Leeuwin Current (Griffiths and Pearce, 1985) and the experiment. The only growth rate reported by Griffiths and Pearce was for their 'structure A' which had $\epsilon/Rf < 0.036$. The experimental value of $\epsilon/Rf = 0.016 \pm 0.005$ is consistent with this observation.

However, in a free surface laboratory experiment we might expect a growth rate closer to the field value.

7. Conclusion

A laboratory model of buoyancy driven coastal currents was produced by differentially heating and cooling the end walls of a rotating rectangular cavity. The currents initially propagated under an alongshore inertial-buoyancy balance and a geostrophic cross-stream balance. After 10 to 15 rotation periods rotational instabilities formed on the edge of the currents. The growth of these structures resulted in a spreading of the flow away from the boundary. At a given cross-section this spreading was roughly linear with time. For small Ekman numbers ($Ek \lesssim 10^{-4}$) and large Froude numbers ($Fr^* \gtrsim 10^3$) the waves produced dipolar eddy structures which coupled with the lower layer. Results indicate that this process slowed the advance of the intrusion. At these small Ekman numbers, the net effect of the Ekman layer beneath the rigid lid was to slow the growth of instabilities, thus *reducing* the decay in the alongshore velocity of the intrusion. On the other hand, at higher Ekman numbers the waves did not break and dissipation in the Ekman layer was directly responsible for any velocity decay. Careful measurements of the instabilities gave quantitative estimates for the wavelength, phase speed and growth rate at small amplitudes.

Comparisons with the Leeuwin Current indicate that the model may be relevant to flow in coastal currents. Quantitative comparisons are remarkably good when one considers that complications such as the continental shelf, external currents and wind stress are absent from the experiment (see McCreary *et al.*, 1986 for a more detailed discussion of these effects). Continuing work on the steady boundary currents and the overall circulation established in the rotating laboratory tank is providing further insight into the nature of coastal currents and the effects of their rotational instability on the mean circulation.

REFERENCES

Chia, F., R. W. Griffiths and P. F. Linden. 1982. Laboratory experiments on fronts. Part II: The formation of eddies at upwelling fronts. Geophys. Astrophys. Fluid Dyn., *19*, 189–206.

Condie, S. A. and G. N. Ivey. 1986. Laboratory experiments on convection in a rotating cavity,

Proceedings of the 9th Australasian Fluid Mechanics Conference Auckland, 8–12 December 1986, 208–210.

Gill, A. E. 1982. Atmosphere-Ocean Dynamics, Academic Press.

Godfrey, J. S. and K. R. Ridgeway. 1985. The large-scale environment of the poleward-flowing Leeuwin Current, Western Australia: Longshore steric height gradients, wind stresses and geostrophic flow. J. Phys. Oceanogr., *15*, 481–495.

Griffiths, R. W. 1986. Gravity currents in rotating systems. Ann. Rev. Fluid Mech., *18*, 59–89.

Griffiths, R. W. and E. J. Hopfinger. 1984. The structure of mesoscale turbulence and horizontal spreading at ocean fronts. Deep-Sea Res., *31*, 245–269.

—— 1983. Gravity currents moving along a lateral boundary in a rotating fluid. J. Fluid Mech., *134*, 357–399.

Griffiths, R. W. and P. F. Linden. 1982. Laboratory experiments on fronts. Part I: Density-driven boundary Currents. Geophys. Astrophys. Fluid Dynamics, *19*, 159–187.

—— 1981. The stability of buoyancy-driven coastal currents. Dyn. Atmos. Oceans, *5*, 281–306.

Griffiths, R. W. and A. F. Pearce. 1985. Instability and eddy pairs on the Leeuwin Current south of Australia. Deep-Sea Res., *32*, 1511–1534.

Ikeda, M., L. A. Mysak, and W. J. Emery. 1984. Observations and modeling of satellite sensed meanders and eddies off Vancouver Island. J. Phys. Oceanogr., *14*, 3–21.

Ivey, G. N. 1987. Boundary mixing in a rotating, stratified fluid. J. Fluid Mech., *183*, 25–44.

Killworth, P. D., N. Paldor and M. E. Stern. 1984. Wave propagation and growth on a surface front in a two-layer geostrophic current. J. Mar. Res., *42*, 761–785.

Killworth, P. D. and M. E. Stern. 1982. Instabilities on density-driven boundary currents. Geophys. Astrophys. Fluid Dynamics, *22*, 1–28.

McCreary, J. P., S. R. Shetye and P. K. Kundu. 1986. Thermohaline forcing of eastern boundary currents: With application to the circulation off the west coast of Australia. J. Mar. Res., *44*, 71–92.

Mysak, L. A. and F. Schott. 1977. Evidence for baroclinic instability off the Norwegian Current. J. Geophys. Res., *82*, 2087–2095.

Narimousa, S. and T. Maxworthy. 1987. Coastal upwelling on a sloping bottom: the formation of plumes, jets and pinched-off cyclones. J. Fluid Mech., *176*, 169–190.

Ou, H. W. 1983. Some two-layer models of the shelf-slope front: Geostrophic adjustment and its maintenance. J. Phys. Oceanogr., *13*, 1798–1808.

Patterson, J. C. and J. Imberger. 1980. Unsteady natural convection in a rectangular cavity. J. Fluid Mech., *100*, 65–86.

Robinson, A. R. (ed.). 1983. Eddies in Marine Science. Springer-Verlag.

Royer, T. C. 1981. Baroclinic transport in the Gulf of Alaska Part II. A fresh water driven coastal current. J. Mar. Res., *39*, 251–266.

Stern, M. E., J. A. Whitehead and B. Hua. 1982. The intrusion of a density current along the coast of a rotating fluid. J. Fluid Mech., *123*, 237–265.

Thompson, R. O. R. Y. 1984. Observations of the Leeuwin Current off Western Australia. J. Phys. Oceanogr., *14*, 623–628.

Wadhams, P., A. E. Gill and P. F. Linden. 1979. Transects by submarine of the East Greenland Polar Front. Deep-Sea Res., *26A*, 1311–1327.